Word Count: 9699 Revision 1

# Gas-mediated trace element incorporation into rhyolite-hosted topaz: a synchrotron microbeam XAS study

**D. R. SCHAUB[1], PAUL NORTHRUP[1], HANNA NEKVASIL[1], TRISTAN CATALANO[1], RYAN TAPPERO[2]**

[1]Department of Geosciences, Stony Brook University, Stony Brook, NY 11794-2100

[2]National Synchrotron Light Source II, Brookhaven National Laboratory, Upton, NY 11973

## ABSTRACT

Magmatic gas exsolving during late-stage cooling of shallow magmas has been considered an important facilitator of low-pressure alteration and metal transport. However, the chemical properties of such gas, particularly its metal transport mechanisms and capacity, remain elusive. Trace elements in minerals produced by gas-mediated surface reaction or precipitation from gas capture details of gas composition and reaction pathways. However, interpretation of mineral trace element contents is dependent on understanding crystallographic controls on gas/mineral partitioning. This work investigates the structural accommodation of As, Mn, Ga, Ge, Fe, and Ti in vapor-deposited topaz of vesicular topaz rhyolite from the Thomas Range, Utah, through single-crystal synchrotron microbeam X-ray techniques on picogram quantities of those trace elements. X-ray absorption near edge structure (XANES) data indicates that these elements are incorporated into topaz as $As^{5+}$, $Fe^{3+}$, $Mn^{3+}$, $Ti^{4+}$, $Ga^{3+}$, and $Ge^{4+}$. Extended X-ray absorption fine structure (EXAFS) analysis for these trace elements, compared to EXAFS of structural Al and Si, reveals that $As^{5+}$ and $Ge^{4+}$ are incorporated directly into the tetrahedral site of the topaz

structure, with the octahedral site accommodating $Mn^{3+}$, $Fe^{3+}$, $Ga^{3+}$, and $Ti^{4+}$. For $As^{5+}$ and $Fe^{3+}$, the structural impact of substitution extends to at least second neighbors (other elements were only resolvable to first neighbors). Further interpretation of the EXAFS results suggests that the substitution of $Ti^{4+}$ results in increased distortion of the octahedral site, while the other trace elements induce more uniform expansion correlating in magnitude to their ionic radius. Comparison of quantified X-ray fluorescence (XRF) data for two topaz crystals from this rhyolite reveals variable trace element concentrations for $As^{5+}$, $Fe^{3+}$, $Ga^{3+}$, and $Ti^{4+}$, reflective of a source gas undersaturated in these trace elements changing in concentration over the period of topaz deposition. The identical $Ge^{4+}$ content of the two topaz crystals suggests that $Ge^{4+}$ in the gas was buffered by the growth of another $Ge^{4+}$-bearing phase, such as quartz. The very low $Mn^{3+}$ content in the topaz crystals does not reflect the abundance of $Mn^{3+}$ in the gas (saturation of Mn is evidenced by coexisting bixbyite). Instead, it suggests a strong Jahn-Teller inhibitory effect to the substitution of $Mn^{3+}$ for $Al^{3+}$ in the distorted octahedral site of topaz. It is proposed that exsolution of an HF-enriched gas from cooling rhyolitic magma led to local scouring of Al, Si, and trace metals from the magma. Once topaz crystals nucleated, self-catalyzed reactions that recycle HF led to continued growth of topaz.

KEYWORDS: crystal structure, EXAFS, igneous rocks, magmatic gas, rhyolite, silicates, single-crystal EXAFS, topaz, trace elements, vapor phase, X-ray absorption spectroscopy

This is the peer-reviewed, final accepted version for American Mineralogist, published by the Mineralogical Society of America.
The published version is subject to change. Cite as Authors (Year) Title. American Mineralogist, in press.
DOI: https://doi.org/10.2138/am-2022-8417. http://www.minsocam.org/

46

47 ## INTRODUCTION

48 Topaz, $Al_2SiO_4(F,OH)_2$, is associated with shallow intrusive domes and lava flows of F-rich
49 rhyolite, specifically, the "topaz rhyolites" of the extensional regions of western North America
50 (e.g., Burt et al. 1982). It is also found in similar rocks cooled at deeper levels, such as rare-earth
51 element enriched pegmatites (e.g., Goad and Černy 1981; Groat et al. 2014) and the plutonic
52 ongonites of eastern Russia and Mongolia (e.g., Kovalenko and Kovalenko 1976). These rocks
53 share the characteristics of high Si, Fe/Mg, and alkali contents; low Ti, Mg, Ca, and P contents;
54 mildly peraluminous character; substantial enrichment of Rb, Cs, Nb, Y, U, Th, Ta, and HREE;
55 and depletion of Eu, Sr, and Co (e.g., Christiansen et al. 1984). Recognition of spatial and
56 genetic links between topaz rhyolite vent complexes and volcanogenic deposits of Be, Li, U, and
57 F (e.g., Lindsey 1977; Bikun 1980; Burt and Sheridan 1981), subvolcanic breccia, porphyry, and
58 greisen deposits of Mo, W, and Sn (e.g., Burt et al. 1982), and F- and Mn-rich base and precious
59 metal veins in volcanic rocks (Bove et al. 2007) (or F-rich skarn replacements in carbonate
60 rocks) make these rhyolites of particular importance.

61 Topaz of nearly F-endmember composition is found in isolated gas cavities and gas vent
62 channels within topaz rhyolites (e.g., Burt et al. 1982). Textural relationships suggest that vapor
63 played an integral role in topaz formation as well as in the formation of the associated quartz,
64 bixbyite, hematite, pseudobrookite, spessartine-almandine garnet, Mn-rich beryl, and cassiterite
65 (e.g., Holfert 1978; Christiansen et al. 1980). The unusual nature of this mineral assemblage, its
66 prevalence in topaz rhyolite, and the chemistry of the rhyolite itself, all suggest that the vapor
67 was sourced from the rhyolite at shallow depths (e.g., Lipman et al. 1969). The minerals in the
68 cavities appear to have been precipitated at high temperature and low pressure (e.g. Roedder and

Stalder 1988) and therefore, may provide insights into F-rich magmatic gas before it has undergone various scrubbing reactions and lost much of its dissolved metal load.

Topaz associated with topaz rhyolite is known to contain trace elements (e.g. Northrup and Reeder 1994; Schott et al. 2003; Wasim et al. 2011; Breiter et al. 2013a; Agangi et al. 2014) that may provide insights into the chemistry of the magmatic gas involved in topaz production. Northrup and Reeder (1994), in their study of the incorporation of trace elements onto growth surfaces of topaz crystals from Mexico, detected Ti, Fe, Ga, Ge, As, and Nb by synchrotron microbeam X-ray fluorescence and noted that these are present in concentrations below approximately 500 ppm. In topaz from an ongonite from Transbaikalia, Russia, Agangi et al. (2014) detected Fe, Na, P, Li, B, Be, Nb, Ta, W, Ga, Ba, and REEs among other trace elements. Both sets of workers concluded that these trace elements were not in inclusions or defects, but rather incorporated into the topaz lattice. Northrup and Reeder (1994) based this conclusion on the uniformity of the cathodoluminescence maps and XRF concentrations of most trace element within subsectors in the crystal and their strict adherence to crystallographic controls. Agangi et al. (2014) based this on smooth time-resolved LAICP-MS signals. However, none of these workers were able to document the incorporation sites of the trace elements in the topaz structure.

The topaz F-endmember, $Al_2SiO_4F_2$, is orthorhombic, with space group Pbnm. Its structure (Alston and West 1928; Pauling 1928; Ribbe and Gibbs 1971) consists of zig-zag chains of edge-sharing $AlO_4F_2$ octahedra along the *c* axis with cross-linking $SiO_4$ tetrahedra (Fig. 1). Adjacent chains of octahedra are rotated 90 degrees relative to each other. Each aluminum octahedron shares two non-opposing O-O edges with adjoining octahedra; the four corners (oxygen ions) defining these edges are also shared with tetrahedra. Fluorine atoms are on adjacent apices of

This is the peer-reviewed, final accepted version for American Mineralogist, published by the Mineralogical Society of America.
The published version is subject to change. Cite as Authors (Year) Title. American Mineralogist, in press.
DOI: https://doi.org/10.2138/am-2022-8417. http://www.minsocam.org/

each octahedron; each F is bonded to 2 Al sites to link adjacent chains (Ribbe and Gibbs 1971). The octahedral site is highly distorted (see Fig. 8 in Northrup and Reeder 1994), with Al-F distances ranging from 1.791 to 1.800 Å and Al-O distances ranging from 1.888 to 1.899 Å. Each $SiO_4$ tetrahedron bridges across the bend of an octahedral chain along c and also cross-links to two adjacent chains. These tetrahedra are somewhat distorted, with Si-O distances ranging from 1.638 to 1.647 Å. Each O in this structure is coordinated to one Si and two Al sites. The $SiO_4$ groups only share corners with octahedra.

In the topaz F-endmember, there is one Al site; however, in partially hydroxylated topaz, there are three unique Al environments whose abundances depend on the relative concentrations of OH and F ($[AlO_4(OH)_2]^{7-}$, $[AlO_4(F)_2]^{7-}$, and $[AlO_4OH,F]^{7-}$) (e.g. O'Bannon and Williams 2019). Unlike topaz from metasediments associated with subduction, which are commonly hydroxylated (e.g. O'Bannon and Williams 2019), topaz associated with topaz rhyolites can be assumed to be compositionally close to the F-endmember. This assumption is supported by early measurements of the refractive index of vapor-deposited topaz from the Thomas Range. Penfield and Minor (1894) analyzed F and $H_2O$ in topaz from the Thomas range and found that the amount of water was minor and the F content was very close to that computed for stoichiometric F-endmember. These workers also observed that the physical and optical properties of topaz vary with the fluorine and water content. Later work by Staatz and Carr (1964) noted that all of the topaz they analyzed from the Thomas Range had similar refractive indices, significantly different from those of topaz associated with more water-rich magmas. Such F-rich topaz is also found in ongonites (Agangi et al. 2014). The increase in F/OH ratio of topaz with formation temperature (Thomas 1982) is consistent with topaz forming early during degassing of topaz rhyolite magma.

Northrup and Reeder (1994) and Agangi et al. (2014) speculated that because the topaz structure is based on a dense packing of anions and has little room for interstitial substitution, trace elements probably substitute for Si or Al. On the basis of size considerations, Northrup and Reeder (1994) predicted that $Fe^{3+}$, $Ga^{3+}$, and $Mn^{3+}$ would replace $Al^{3+}$ in the topaz structure, while $Ge^{4+}$ would substitute for $Si^{4+}$. Since $Ti^{4+}$ is too large for the Si tetrahedron they suggested that it substitutes for $Al^{3+}$ with charge compensation occurring through substitution of $O^{2-}$ for $F^{-}$. Similarly, they predicted that $Nb^{5+}$ would replace $Al^{3+}$ with a coupled substitution of $2O^{2-}$ for $2F^{-}$. The complexities of As substitution are compounded by its unknown valence state in topaz. Northrup et al. (1995) reported preliminary As EXAFS results on powdered topaz from a Mexican topaz rhyolite and concluded that As was incorporated into topaz as tetrahedrally coordinated $As^{5+}$, with an As-O distance of 1.70 (0.02) Å. However, as this was a bulk measurement, they were unable to definitively identify topaz as the host of this As. Based on simple charge balance considerations, Agangi et al. (2014) suggested that trace element incorporation was primarily valence-based, for example, replacement of Si by other cations in the 4+ oxidation state (Ti, V), and replacement of $Al^{3+}$ by 3+ cations (Ga, Fe, Mn). Uptake of Nb, Ta, and W, which usually occur in the 5+ oxidation state, would require coupled substitution.

In order to clarify the structural accommodation of As, Mn, Ga, Ge, Fe, and Ti in F-rich topaz, we obtained detailed information on their crystallographic environment through synchrotron-based XAFS (X-ray absorption fine structure) investigation of single-crystal topaz at microbeam resolution. Data collection spanned the XANES (X-Ray Absorption Near Edge Structure) and EXAFS (Extended X-ray Absorption Fine Structure) regions. XAFS probes the details of how X-rays are absorbed by an atom at energies near and above the core-level binding

energies of that atom. The XANES region is sensitive to oxidation state and coordination chemistry of the absorbing atom; the EXAFS region provides details about an element's local structure (within ~10 Å) in crystalline or non-crystalline materials (e.g., the distances, coordination number, and species of the neighbors of the absorbing atom, Newville 2008). For this investigation, we used the hard X-ray microprobe, XFM (which accesses elements from Ca to Zr using their K absorption edges and heavier elements using their L edges) and the tender-energy microprobe TES (Northrup 2019) (which provides unique access to lighter elements Mg through Ca) at NSLS-II; details below.

## ANALYTICAL PROCEDURE

### Sample characteristics and preparation

The topaz crystal studied here by XAS (Topaz-64) is from Topaz Mountain of the Thomas Range, Utah. The sample is geologically young (6-7 Ma based on the age of the rhyolite; Lindsey 1982). It is 4x6x24 mm in length (along the a, b, and c axes, respectively), and is dominated by (110), with lesser forms (112), (002), (020), (111), (112) and (101) (Fig. 2). A smaller topaz crystal (2x4x14 mm) is attached; this crystal supports a partially embedded 1mm bixbyite ($Mn_2O_3$) cube. The lower part of the doubly-terminated main crystal encases concentric layers of small quartz crystals and fine-grained rhyolitic matrix. The crystal is transparent with large areas free from visible inclusions. It has pristine surfaces including sharply defined polygonized growth hillocks, indicating the absence of fluid interaction subsequent to crystal formation. Its light sherry color indicates that the crystal was not subjected to heat or exposed to sunlight as either process would render it colorless (e.g., Rossman 2011). The pristine nature of this crystal suggests that it preserves its original trace element budget.

This is the peer-reviewed, final accepted version for American Mineralogist, published by the Mineralogical Society of America.
The published version is subject to change. Cite as Authors (Year) Title. American Mineralogist, in press.
DOI: https://doi.org/10.2138/am-2022-8417. http://www.minsocam.org/

The area chosen for analysis lies on a large (3x9 mm) polygonized growth hillock on one of the (110) faces (similar to the hillocks studied by Northrup and Reeder 1994, 1995). This surface has growth steps aligned along [001] and [110]. For analysis, the sample was mounted intact onto a standard 2"x2" frame such that the (110) surface faced the beam at 45 degrees and was in the x-y plane of the sample stage, and the *c* axis was vertical. Initial X-ray fluorescence survey maps (e.g. Fig. S1) were used to identify an area of uniform composition, free from oxide inclusions that may be rich in the trace elements of interest. The volume of topaz accessed for each element was defined by a beam size of ~10 μm with an effective sampling depth of 10-150 μm depending on incident beam and fluorescence photon energies.

**Beamline setup**

The optical setup for the XFM hard X-ray microprobe from its three-pole-wiggler broadband source consists first of a horizontal toroidal focusing mirror to gather pink beam to a secondary source aperture (SSA). The beam diverging from the SSA is then vertically collimated by a bent flat mirror and monochromated by a fixed-exit Si(111) double-crystal monochromator. A secondary microfocus is produced by use of an orthogonal pair of dynamically bent mirrors in KB geometry, such that beam size at the sample can be adjusted from 2 to 10 μm by adjusting the SSA size at the expense of flux. Samples are mounted on a fine-resolution x-y scanning stage at 45 degrees to the incident beam, so that the sample surface can be raster-scanned with respect to the fixed beam. A 4-element Si drift detector is located in the horizontal plane at 45 degrees to the sample (90 degrees to the incident beam to minimize scatter) to capture fluorescence from the sample. Fluorescence signal is processed by selecting element-specific fluorescence energies and normalizing to incident beam intensity as measured by an ionization chamber upstream of the microfocusing mirrors.

This is the peer-reviewed, final accepted version for American Mineralogist, published by the Mineralogical Society of America.
The published version is subject to change. Cite as Authors (Year) Title. American Mineralogist, in press.
DOI: https://doi.org/10.2138/am-2022-8417. http://www.minsocam.org/

The optical setup at the TES tender-energy microprobe beamline (Northrup 2019), co-designed as the lower-energy sister beamline to XFM at NSLS-II, consists of a bend-magnet source, vertically collimating mirror pair, fixed-exit double-crystal monochromator, and vertically deflecting toroidal mirror focusing to an SSA; beam diverging from the SSA is refocused by a custom set of KB mirrors to a user-tunable spot size of 2 to 10 μm. The sample chamber environment is helium at 1 atm pressure. Sample stage and detector geometry is the same as for XFM; fluorescence is measured using a Ge detector optimized for this energy range. This geometry, including the KB endstation and monochromator now at TES, was prototyped at NSLS Beamline X15B. The Al EXAFS and Si EXAFS reported here were measured at X15B; Si XANES and additional Si EXAFS were measured at TES. Si measurements used InSb monochromator crystals; Al measurements used beryl ($Be_3Al_2Si_6O_{18}$) crystals.

**Data collection**

XRF spectra were collected and summed over selected regions of a small (100 x 100 μm) area of Topaz-64, and of an additional topaz crystal from the same locality (Topaz-7), for comparison with concentration standards measured under identical geometric conditions. These standards are thin films of elements deposited on a polymer substrate with controlled mass per unit area, so there is no thickness effect on fluorescence, only the effects of layer ordering and of absorption by layers above the element of interest. Reference films used were NIST 1833 Serial No. 991 for Fe and Ti, NIST 1832 Serial No. 1294 for Mn, and MicroMatter 41156 for As and Ga.

XAS spectra for Topaz-64 were obtained by scanning incident beam energy across each element's K absorption edge while measuring fluorescence (which is directly proportional to absorption). Energy steps were larger in the pre-edge background and post-edge regions, and

205 smaller over the absorption edge in order to capture edge position and detailed features of
206 XANES. For EXAFS, a longer post-edge range was measured in steps calculated in constant k.
207 EXAFS measurements of all trace elements were made in the same area of the crystal (within a
208 radius of 150 μm) and in the same geometric orientation (Table S1 in Supplementary Material
209 provides XAS scan parameters used for each element). Fresh spots within this area were used for
210 each redox-sensitive element, to minimize the chance for radiation-induced changes. Spectra
211 were also monitored scan-to-scan for any indication of progressive changes; no evidence for
212 beam-induced change was observed for any of these measurements.

213 The approach adopted here, microbeam XAS of a single crystal, was necessary to enable
214 probing of microscale regions free of inclusions, but there are drawbacks to this approach that
215 must be carefully identified and mitigated. XANES and EXAFS measurements of a single crystal
216 will be sensitive to crystal orientation relative to the horizontal polarization of the incident beam
217 (e.g. Dyar et al. 2016). All single-crystal measurements reported here were collected with the
218 crystal in the same orientation relative to the beam in order to minimize the effects of
219 orientation-dependence. The amplitude (probability of occurrence) of each individual scattering
220 path will vary with its orientation. Scattering paths oriented vertically are least represented. This
221 limitation is mitigated by the grouping of paths into shells, and into sets of shells sharing
222 parameters, as discussed below. This grouping averages over a large number of paths, providing
223 a sufficient distribution to minimize orientation effects impacting individual paths. We
224 specifically chose the orientation of the sample, with the (110) plane at 45 degrees to the beam
225 and *c* axis vertical, because in the topaz structure that orientation gives a fairly well-averaged
226 representation of the different paths. In topaz, the crankshaft-like chains along the *c* axis (Fig. 1)
227 effectively distribute most paths away from the vertical [001] vector. The symmetry of topaz

This is the peer-reviewed, final accepted version for American Mineralogist, published by the Mineralogical Society of America.
The published version is subject to change. Cite as Authors (Year) Title. American Mineralogist, in press.
DOI: https://doi.org/10.2138/am-2022-8417. http://www.minsocam.org/

indicates that sub-units alternate by 90 degrees in orientation perpendicular to the *c* axis, further averaging the orientation effects for the chosen orientation. This averaging was confirmed by the similarity between Si EXAFS of both powdered and single-crystal samples. Finally, all measurements of trace elements, and the Si reference EXAFS, were done in exactly the same orientation, validating the direct comparisons presented in this work.

For a baseline measurement of the topaz host structure, we also measured Si K-edge XANES and EXAFS of the same crystal in the same orientation, utilizing a 0.5 mm diameter beam in an area free from quartz inclusions (the larger area for these measurements is justified because any metal oxide inclusions will not contribute to the Si signal). Because the Al content limited sampling depth for Si XAS, there was no issue with self-absorption effects as might otherwise occur in an "infinitely thick" sample. For the octahedral site, we measured Al K-edge EXAFS of a powdered sample of F-topaz from a topaz rhyolite near Tepetates, San Luis Potosi, Mexico. Measurement of Al EXAFS is challenging, and further complicated by the Al-bearing beryl monochromator crystals which precluded measurement near the Al K-edge. Therefore, we were only able to measure EXAFS, not XANES, and there is inherently more uncertainty in the Al fitting results.

## DATA PROCESSING

### Trace element concentrations

Quantitative trace element concentrations were obtained by comparison of XRF maps of the sample and thin-film standards. For each element, fluorescence intensity of the standard was corrected for attenuation and converted to mass per unit area. This value was ratioed with fluorescence intensity in the sample and converted to mass per unit volume using a computed

sampling depth (e.g. Citrin et al. 1998) with absorption data from the CXRO tool (https://henke.lbl.gov/optical_constants/atten2.html). In the absence of a reference material for Ge, the concentration was computed indirectly using a standardless method in which As concentration served as the effective standard. Germanium fluorescence intensity was ratioed to arsenic, with corrections for sampling depth, fluorescence efficiency, and absorption by the air path and detector window. The fluorescence energies of As and Ge are similar, so the corrections in the Ge calculation were relatively small.

**μ-XAS spectra**

The Demeter software suite (Ravel and Newville 2005) was used to process the XAS spectra. Processing started with data assessment and compilation with the Athena module. Data obtained from four detector channels were recorded; however, scans from one channel were removed from the As, Ga, and Ge data sets due to prominent diffraction artifacts spanning the data set. Individual scans were also screened for any glitches affecting more than a few energy data points, resulting in further exclusion of a handful of scans per element. After these exclusions, the usable number of scans for each element was as follows: As, 102; Fe, 61; Mn, 7; Ge, 10; Ga, 3; Ti, 38. The set of scans for each element was then merged and any remaining minor glitches edited out. Finally, pre- and post-edge (line and spline function) backgrounds were subtracted, edge steps were normalized to 1, and the Fourier transform Rbkg parameter set to 0.85 or 0.8 for each element based on the expected bond lengths for the substitution sites.

Our approach to the analysis of the μ-XAS spectra takes advantage of knowledge of the topaz structure, which provides a starting model for the two candidate cation sites. Therefore, despite the limitations of microbeam data quality and the complexities arising from orientation dependence, we are still able to address the questions of site assignment and local distortion.

**XANES.** Initial analysis of the merged XAS spectra focused on the X-ray absorption near edge structure (XANES) region. The energy position of the absorption edge of a spectrum is characteristic for a particular valence state of an element. Therefore, comparison of measured spectra with those of materials with known valence is a straightforward diagnostic tool to determine the charge of the measured element. The valence, in turn, informs preliminary assignment of the cation's structural environment, in this case tetrahedral (the Si site) or octahedral (Al site) coordination. For elements with multiple possible oxidation states (Fe, Mn, As), the XANES region of each element's merged spectrum was compared with XANES spectra of reference standards measured under appropriate similar conditions at XFM to determine their oxidation state in topaz.

**EXAFS.** The merged spectra were input into the Artemis software module to determine the effect of trace element substitutions on interatomic distances. For each trace element, baseline scattering paths were calculated from trace element-free fluor-topaz crystal structure parameters of Northrup et al. (1994) by the Artemis FEFF utility, with the trace element atom substituted for Si or Al as the absorbing atom in the distorted tetrahedral or octahedral site, respectively. These paths are equivalent to the interatomic distances between the element of interest and a nearby neighbor (i.e., bond length in the case of nearest-neighbors).

For fitting, single-scattering paths from the trace element of interest were grouped into shells of similar path length (for example, the oxygen anions of the tetrahedral site comprised one shell). The geometry of the crystal was 'frozen' except for linear expansion of these paths. Fitting parameters for deviation in path length compared to the baseline crystallographic model ($\Delta R$), amplitude reduction ($S0^2$), and sigma squared disorder parameters ($\sigma^2$) were assigned on a per-shell basis. Separate amplitude reduction variables were needed for each shell to account for

orientation effects arising from measurement of an oriented single crystal. It is important to note that individual scattering paths were preserved, with the shell ΔR applied uniformly to each path within a shell. In this way, we evaluated the overall distortion of the local structure to accommodate the trace element, while significantly reducing the number of variables. This simplified fitting model limits interpretation at the scale of individual bonds but is sufficient to conclusively determine the crystallographic site hosting each trace element and to evaluate overall structural accommodations.

Shells were fit sequentially, continuing outward from the absorbing atom until data quality precluded further fitting. For the octahedral site, inclusion of both oxygen and fluorine paths in the first shell generally yielded a better fit than treating them separately. Most fits included one shell beyond the results reported here, as the overlapping contributions from the outermost shell usually improved the fit of inner shells, even when the outer shell could not be well-fitted due to poorly resolved data. Notes on these partial fits, as well as any special considerations for individual elements, are presented in the results section for each element.

# RESULTS

## Trace element abundances

Table 1 shows the calculated concentration of each trace element, and corresponding mass exposed to the X-ray beam. For Topaz-64, arsenic was most abundant at 327 ppm, equivalent to ~12.5 pg within the sample volume analyzed, allowing for well-resolved As XAS spectra. In contrast, manganese spectra were the most difficult to resolve due to a concentration of only 9 ppm, or ~0.1 pg in the sample volume.

## XAS results

This is the peer-reviewed, final accepted version for American Mineralogist, published by the Mineralogical Society of America.
The published version is subject to change. Cite as Authors (Year) Title. American Mineralogist, in press.
DOI: https://doi.org/10.2138/am-2022-8417. http://www.minsocam.org/

The merged, deglitched XAS spectra for the trace elements studied in Topaz-64 are shown in Figure 3 (black spectra, XANES region) and Figure S2 (full spectra). These spectra were used for XANES and EXAFS analysis.

**Trace element valence states determined by XANES.** The topaz trace element XANES spectra were compared to reference sample spectra (Fig. 3) measured at XFM for known oxidation states. The As merged spectrum absorption edge position shows a clear match to $As^{5+}$. Comparison of Fe spectra suggests Fe incorporation into topaz as ferric iron. The absorption edge position of the Mn merged spectrum offers the best agreement with $Mn^{3+}$, consistent with the coexisting bixbyite ($(Mn,Fe)_2O_3$). No valence standards were available for Ga, Ge, or Ti. Gallium and germanium are expected to be present as $Ga^{3+}$ and $Ge^{4+}$. The titanium was identifiable as $Ti^{4+}$ due to the presence of a diagnostic double-peaked pre-edge feature (e.g. Farges et al. 1997).

XANES also offers a preliminary assignment of crystallographic sites for these substituents. Although oxidation state is a first-order indicator of crystallographic site, the overall shape and minor features of the XANES spectra can also be indicators as they reflect differences in coordination, symmetry and crystal field. For example, as can be seen in Fig. 3, the overall spectral shapes of As (Fig 3a) and Ge (Fig. 3b) are very similar to that of Si (Fig. 3b inset). These differ from the other XANES spectra, which are more generally similar to each other. On that basis, As and Ge likely occupy the tetrahedral site, while Fe, Mn, Ti and Ga may occupy the octahedral site. The pre-edge peak height of the titanium is consistent with octahedral coordination (Farges et al. 1997).

**Impact of trace element incorporation on local bonding and geometry.** EXAFS was used to definitively identify site assignments, and to assess the effect of incorporation of the trace

elements studied on local bonding and geometry in the topaz structure. The first step in EXAFS analysis is conversion of energy data (Fig. S2) to frequency (k), and Fourier transformation to R for each element (Figs. 4, 5, 6). The position of the first-shell peak and overall combination of peaks in R (radial distance uncorrected for phase shift) yield characteristic visual fingerprints for tetrahedral and octahedral substitution sites in topaz. This allows provisional differentiation between the tetrahedral and octahedral sites for each trace element even before fitting efforts. Based on the peaks in R, the tetrahedral site contains $As^{5+}$ and $Ge^{4+}$ and the octahedral site $Mn^{3+}$, $Fe^{3+}$, $Ga^{3+}$, and $Ti^{4+}$. These assignments were confirmed by attempting to fit the data to each site model and ruling out the unresolvable fit for each element.

Extraction of interatomic distances from EXAFS data starts with the closest coordinated anions (first shell) and proceeds to nearest neighbor cations (second shell) and a set of anions associated with those cations (third shell) as data quality permits. For this data set, acceptable fits could only be obtained out to the first or second shell, due primarily to the extremely low concentrations of most elements analyzed. To improve the quality of reported fits, and because we have independent knowledge of the host structure, fitting was generally carried out to one shell beyond the presented results. While these outer shells could not be fully resolved, they make small but significant contributions to the overall fit. In some cases, fits generated invalid negative sigma squared values. As long as the values could be positive within the uncertainty, however, we accepted these as a side effect of the somewhat disparate path lengths included within some shells compounded by orientation dependence effects.

Determining the effects of trace element substitution on the topaz structure requires comparing the calculated interatomic distances from the trace element of interest to its neighbors with those of the unsubstituted cation (Al or Si) and its neighbors. To assist in these

364 comparisons, Si and Al EXAFS data were collected for the sample and fitted in the same manner
365 as the trace elements. Figure 4 shows the fits for Si and Al.

366 Table 2 shows the path lengths (R) from prior crystallographic data (single-crystal X-ray
367 diffraction; Northrup et al. 1994) and those computed from the Si and Al EXAFS fits. The Al
368 results are of particular note, as Al in the beryl monochromator crystals used for this energy
369 range makes this measurement extremely difficult to obtain. We believe this to be the first
370 reported Al k-edge EXAFS data for topaz. Variations in path length between the crystallographic
371 model and this EXAFS fit were minimal and within the uncertainty of the fitting parameters for
372 both Si and Al. The somewhat higher values of $\sigma^2$ (the disorder parameter) for the Al fit is to be
373 expected given the wider spread of path lengths grouped into each shell and high correlation with
374 the $SO^2$ (amplitude reduction) parameter. Low $SO^2$ values for the second shells are also not
375 unexpected and are presumed to result primarily from orientation dependence resulting from
376 taking measurements on a single crystal.

377 **Accommodation of trace elements in tetrahedral coordination.** Figure 5 shows the
378 EXAFS data and fit for arsenic. Fitting of the merged As spectrum was carried out to the third
379 shell, although only the first and second were fully resolvable. Interatomic distances between As
380 and its first and second shell neighbors increased by ~0.06 Å compared with the unsubstituted
381 model structure (Table 3).

382 The germanium dataset proved challenging due to its low concentration in the topaz and
383 fewer usable scans. Figure 6 shows R of the Ge data and fit of the first shell. A second shell was
384 incorporated into the fit calculations so that the shoulder underlying the first shell peak could be
385 accounted for. The fit generated a first shell $\Delta R$ of 0.092 Å (Table 3).

This is the peer-reviewed, final accepted version for American Mineralogist, published by the Mineralogical Society of America.
The published version is subject to change. Cite as Authors (Year) Title. American Mineralogist, in press.
DOI: https://doi.org/10.2138/am-2022-8417. http://www.minsocam.org/

**Accommodation of trace elements in octahedral coordination.** In the octahedral site, as had been observed for the Al fitting, the fits for the elements resulted in somewhat lower $S0^2$ values. This lends support to the suggestion that these values are predominantly a result of orientation effects rather than an issue with data quality or specific to an element. Second shell fits were more difficult in general; this is due to the larger spread of path lengths contained within the second shell, and their substantial overlap and possible destructive interference with the paths of the third shell.

Figure 7 shows the data and fits in R for octahedral Fe, Ga, Mn, and Ti. Iron was fitted to the nearest-neighbor silicon sites (second shell) with an unresolvable third shell. Table 4 shows the computed interatomic distances. The fit produced a first shell ΔR of 0.086 Å and a second shell ΔR of 0.021 Å. The Mn fit resulted in a first shell ΔR of 0.034 Å. The second shell of Mn proved difficult. Gallium was fit out to the third shell, though here we limited the number of variables by sharing fitting variables between the second and third shells. Only the resulting first shell is reported, with a ΔR of 0.022 Å.

The Ti fit proved uniquely challenging; a first shell fit of acceptable quality could not be obtained until the shorter Ti-F paths and longer Ti-O paths were allowed to vary independently of each other in ΔR. This resulted in a Ti-F ΔR of .042 Å and a Ti-O ΔR of .113 Å, nearly doubling the difference in distance between these sites compared to the aluminum and indicating a substantial non-uniform distortion of the octahedron and possibly strengthening of one or both bonds to the F site (the ΔR is less than the increase in ionic radius from $Al^{3+}$ to $Ti^{4+}$). This is consistent with substitution of O for F in one or both of these sites to satisfy the increased bonding requirement and charge balance for $Ti^{4+}$. Fitting beyond the first shell was not possible, likely due to compounded effects of this increased distortion of the octahedral site.

This is the peer-reviewed, final accepted version for American Mineralogist, published by the Mineralogical Society of America.
The published version is subject to change. Cite as Authors (Year) Title. American Mineralogist, in press.
DOI: https://doi.org/10.2138/am-2022-8417. http://www.minsocam.org/

## TOPAZ FORMATION AND GAS CHEMISTRY

**Topaz formation.** Formation of topaz in cavities in topaz rhyolite most likely involved a gas phase. The presence of gas is consistent with the cavities found in the rhyolites and the observation that crystals grew away from the rock interface and toward the cavity and spiral-growth hillocks formed on surfaces not in contact with the rhyolite. The most reasonable source for this gas is local, that is, the rhyolitic magma itself. Topaz formation can be envisioned as resulting from either (i) direct deposition from the cooling gas or (ii) localized reaction of exsolved gas with the solidified or almost solidified rhyolite. Method (i) requires a significant transported load in order to produce large crystals in small cavities. Considering gas density and the low solubility of the gaseous species needed for topaz growth (specifically Si and Al), a large flow-through volume would be needed to provide the mass of the observed crystals. Method (ii) can be accomplished by exsolved gas with high HF content and low transported load through a continuous cycle of local dissolution and precipitation that can temporarily mobilize species with low solubility in the gas and redistribute them while retaining HF in the gas. This is supported by observation of concentric etching of the host rhyolite surrounding the original cavity as evidenced by residual layers of drusy quartz crystals lining the cavity, with subsequent growth of the topaz crystal into both the cavity and the etched regions. The following reactions may define topaz formation:

$$4HF\ (gas) + SiO_2\ (rhyolite) \Rightarrow SiF_4\ (gas) + 2H_2O\ (gas)$$

$$6HF\ (gas) + Al_2O_3\ (rhyolite) \Rightarrow Al_2F_6\ (gas) + 3H_2O\ (gas)$$

$$SiF_4\ (gas) + 4H_2O\ (gas) \Leftrightarrow Si(OH)_4\ (gas) + 4HF\ (gas)\ (gas\text{-}phase\ equilibrium)$$

$$Si(OH)_4\ (gas) + Al_2F_6\ (gas) \Rightarrow Al_2SiO_4(F_2)\ (topaz) + 4HF\ (gas)$$

Once a topaz crystal has nucleated, however, self-catalyzed surface reactions that recycle HF would likely dominate. In these, –AlF on the growing surface of the topaz could react with $Si(OH)_4$ (gas) to form an Al-O-Si bond and release HF. Subsequently, –SiOH on the surface could react with $Al_2F_6$ (gas) and produce a Si-O-Al bond and release HF. This process could lead to rapid growth of the observed large crystals of topaz in relatively small cavities.

The sum of the reactions given above would result in a net loss of 2HF (gas) and a net production of $1H_2O$ (gas) per formula unit of topaz. This would eventually deplete the HF in the gas. However, it is known that F partitions strongly into the melt in magmatic systems. Release of F from the rhyolite may be limited by availability of water if HF is the primary F-bearing gaseous species. Since the topaz-forming reactions produce $H_2O$, we can add the following reaction to maintain HF content in the gas, as this $H_2O$ reacts with remaining F in the rhyolite:

$$H_2O\ (gas) + 2F^-\ (rhyolite) => 2HF\ (gas) + O^{2-}\ (rhyolite)$$

This reaction could occur as the rhyolite is etched in the above process when temperatures are still 500-700°C, and would buffer the gas $HF/H_2O$ ratio, allowing the topaz-forming reaction to continue under steady-state gas composition as long as feedstock remains available and reaction conditions (e.g. temperature) are maintained. One final consideration is that there is a parallel reaction that produces quartz:

$$Si(OH)_4\ (gas) => SiO_2\ (solid) + 2H_2O\ (gas)$$

This reaction provides an independent mechanism to buffer the Si content in the gas, as topaz crystallizes and the rhyolite feedstock is consumed.

**Insights into the gas.** The topaz analyzed in this study indicates that the gas involved in its production was able to mobilize $As^{5+}$, $Fe^{3+}$, $Mn^{3+}$, $Ti^{4+}$, $Ga^{3+}$, and $Ge^{4+}$ in addition to Al and Si.

453 XANES and EXAFS analysis showed that each of these trace elements are incorporated into the
454 fluor-topaz structure, with the tetrahedral site containing $As^{5+}$ and $Ge^{4+}$ and the octahedral site
455 $Mn^{3+}$, $Fe^{3+}$, $Ga^{3+}$, and $Ti^{4+}$.

456 Although trivalent arsenic is the dominant oxidation state in basaltic glass at 1200 $^{o}$C, with
457 pentavalent As contributing less than 10% of the budget of As (Maciag and Brenan 2020), at
458 lower T and high $fO_2$, the pentavalent state is more abundant (Verweij 1980) with $As^{5+}$ species
459 such as $AsO_4^{3-}$ in the melt. If these are also prevalent in rhyolite, then in the presence of $H_2O$
460 (gas) at the surface of the rhyolite, these species may become hydrated to form $AsO(OH)_3$.
461 Studies of speciation and structure of As in natural melts and glasses suggest that such oxy-
462 hydroxide complexes form strong bonds within the rhyolite glass and solids. High HF contents
463 may be necessary to release these to the gas (e.g., Pokrovski et al. 2002; Testemale et al. 2004;
464 Borisova et al. 2010; James-Smith et al. 2010). Local transport of released $AsO(OH)_3$ and
465 precipitation of As in topaz by an HF-rich gas can be envisioned by the reaction:

466 $$AsO(OH)_3\ (gas) + Al_2F_6\ (gas) + H_2O\ (gas) \Rightarrow Al_2AsO_4(FO)\ (topaz) + 5HF\ (gas)$$

467 although it is more likely that -Al-F species on the surface of the growing topaz react with
468 $AsO(OH)_3$. This reaction reflects the coupled substitution needed for $As^{5+}$ to substitute for $Si^{4+}$ in
469 the tetrahedral site, most likely the substitution of an $O^{2-}$ for $F^-$ (or $OH^-$) at one of the two "F
470 apices" of a neighboring octahedron (Fig. 1) for charge balance. In spite of the required coupled
471 substitution, the As content (327±16 ppm) is the highest of all of the trace elements analyzed
472 here in Topaz-64 (Table 1). Arsenic contents in topaz can be quite variable, however. Table 1
473 also shows the trace element content of Topaz-7; its arsenic concentration is only 20±1 ppm.
474 This difference in As content could be explained by topaz with lower As growing earlier, since a
475 higher As content in the gas would result from continued precipitation of non-As bearing phases.

476 Like $As^{5+}$, $Ge^{4+}$ substitutes for Si, although its slightly greater ionic radius induces a slightly
477 greater expansion of the structure upon substitution (as indicated by the slightly longer Ge-O
478 bond relative to the As-O bond in Table 3). The similarity in size of $As^{5+}$ and $Ge^{4+}$ and their joint
479 preference for the tetrahedral site, however, suggest that their solubilities in topaz should be
480 similar. Therefore, the much lower $Ge^{4+}$ content (14.8±0.7 ppm, Topaz-64; 14.5±0.7 ppm, Topaz
481 7) compared with $As^{5+}$ content (327±16 ppm, Topaz-64) suggests several possibilities: (i) that
482 the gas may not have inherited much Ge from the rhyolite source, (ii) the $Ge^{4+}$ content of the gas
483 was being buffered by the presence of a condensed phase, leading to a concentration far below
484 saturation, or (iii) for some unknown reason, the tetrahedral site in topaz cannot accommodate
485 much $Ge^{4+}$. Breiter et al. (2013b) documented $Ge^{4+}$ contents as high as 204 ppm in topaz, that is,
486 much closer to what we observed for $As^{5+}$. This excludes (iii) and is consistent with a similar
487 partitioning potential of $As^{5+}$ and $Ge^{4+}$ into topaz. Although only 2 topaz crystals were analyzed
488 here – too few to draw a robust conclusion – (ii) seems most likely, as the same concentration of
489 $Ge^{4+}$ in both crystals suggests that the Ge concentration in the two topaz crystals analyzed was
490 buffered through the precipitation of another Ge-bearing mineral phase in which $a_{Ge}^{S} \ll 1$, such
491 as quartz, magnetite (e.g., Meng et al. 2017), hematite (e.g., Bernstein and Waychunas 1987),
492 cassiterite, or bixbyite (see summary of Höll et al. 2007). All of these phases have been found
493 associated with topaz rhyolite (Burt et al. 1982**;** Christiansen et al. 1984). In fact, as noted above,
494 a crystal of bixbyite was attached to one of the topaz samples analyzed here (Fig. 2) and quartz
495 was associated with both samples. Such buffering of $Ge^{4+}$ activity would inhibit the relative $Ge^{4+}$
496 content of the gas from increasing much during precipitation of nominally Ge-free phases.

497 Of the trace elements preferentially partitioning into the octahedral site, $Fe^{3+}$ has the greatest
498 abundance in the topaz crystals analyzed. The structural effects of $Fe^{3+}$ substitution diminish

499 further away from the cation (Table 4). These observations suggest primarily an effect of larger
500 ionic radius with little distortion of the structure. Formation of the $Fe^{3+}$ topaz component is likely
501 facilitated through the reaction of HF with the rhyolite, perhaps through the following reactions:

502 $$6HF\ (gas) + Fe_2O_3\ (rhyolite) \Rightarrow Fe_2F_6\ (gas) + 3H_2O\ (gas)$$

503 $$Si(OH)_4\ (gas) + Fe_2F_6\ (gas) \Rightarrow Fe_2SiO_4(F_2)\ (topaz) + 4HF\ (gas)$$

504 This topaz component may also be formed by -Si-O on the topaz surface reacting locally with
505 $Fe_2F_6$ in the gas. Although the Fe concentrations in the topaz crystals analyzed are high ($Fe^{3+}$:
506 288±9 ppm, Topaz-64; 158±5 ppm, Topaz-7), they do not approach the more than 400 ppm of
507 $Fe^{3+}$ that has been observed in other topaz crystals (Breiter et al. 2013b). This suggests that when
508 this topaz formed, hematite was not yet precipitating and that the ferric iron content of the gas
509 continued to increase during formation of Fe-poor precipitates.

510 The minor perturbation of the topaz structure by $Ga^{3+}$ and $Mn^{3+}$ substitution for $Al^{3+}$ (Table
511 4) suggests that topaz should be able to accommodate a significant amount of both. The much
512 lower concentration of $Ga^{3+}$ than $Fe^{3+}$ for both crystals analyzed suggests a lower $Ga^{3+}$
513 concentration in the rhyolite source, consistent with generally low Ga contents of felsic rocks
514 (e.g., Breiter et al. 2013b) and possibly coupled with lower partitioning of $Ga^{3+}$ into the gas. The
515 much lower $Mn^{3+}$ abundance relative to $Fe^{3+}$ is more difficult to explain since the presence of co-
516 existing bixbyite in Topaz-64 suggests a high load of Mn locally in the gas and that Topaz-64
517 was saturated in Mn. The low concentration of Mn in topaz at saturation with bixbyite may be
518 caused by the symmetry-lowering Jahn-Teller distortion of $Mn^{3+}$ in octahedral coordination (e.g.,
519 Halcrow 2013; Fridrichová et al. 2018). This Jahn-Teller distortion is likely incompatible with
520 the octahedral distortion inherent to the topaz structure caused by two shorter F apices and may
521 thus reduce the compatibility of Mn with the topaz structure, leading to a low solubility. In

522 comparison, beryl, formed under similar conditions in topaz rhyolite, but with a less distorted
523 $AlO_6$ octahedral site, can incorporate much higher Mn contents (e.g., Sardi and Heimann 2014;
524 over 300 ppm $Mn^{3+}$ in a beryl from Utah topaz rhyolite measured for this work). The low
525 solubility of Mn in topaz observed here is consistent with the typical low Mn contents for topaz
526 from anorogenic granite (Breiter et al. 2013b).

527 $Ti^{4+}$ substitution for Al in the octahedral site in topaz must be a coupled substitution in which
528 one of the apical $F^-$ (or $OH^-$) ions of the octahedron is replaced by $O^{2-}$ for charge balance. As
529 shown in Table 4, the cation-F bond in the octahedron is shorter than the cation-O bond. In a
530 fully relaxed structure, the substitution of $O^{2-}$ for $F^-$ (or $OH^-$) would thus lengthen the bond, but
531 the topaz structure does not permit this and the Ti-O bond in a F site will remain shortened. This
532 is effectively a Ti=O double bond, common in Ti-bearing phases (e.g., titanite, Speer and Gibbs
533 1976), which satisfies the increased bonding needs for $Ti^{4+}$ in that site.

534 In late-stage rhyolite melt $Ti^{4+}$ may be in 5-coordinated complexes with 4 bridging and one
535 non-bridging O bond (e.g., Ackerson et al. 2020) that are tightly bound and likely show little
536 solubility in the exsolving gas. This may account for the observation that Ti abundance is low in
537 the gas phase (e.g., Symonds and Reed 1993; Shevko et al. 2018). In spite of these complexities,
538 $Ti^{4+}$ contents are quite variable in topaz, and can reach 480 ppm (Gauzzi and Graça 2018),
539 suggesting that the Ti contents in the topaz studied here, had not reached saturation in $Ti^{4+}$
540 content.

541 Perhaps in spite of low Ti solubility in gas, locally, reaction of an HF-rich gas with Ti-
542 bearing rhyolitic glass, ilmenite (or hematite with an ilmenite component) could release $Ti^{4+}$ to
543 form a gaseous species such as $TiF_4$. This may produce the Ti topaz component through a
544 reaction such as:

545 $Si(OH)_4$ (gas) + $2TiF_4$ (gas) + $2H_2O$ (gas) = $Ti_2SiO_4(OO)$ (topaz) + 8HF (gas)

546

547 ## IMPLICATIONS

548 This work has demonstrated that synchrotron-based microbeam XAS studies on picogram
549 abundances of trace elements in single crystals can yield definitive information on their
550 oxidation states, site occupancy, and the local structural perturbations that they induce. It
551 documents the substitution of arsenic for silicon in a common silicate mineral. This work also
552 presents the first synchrotron-based Al EXAFS analysis of topaz. In addition to improving our
553 understanding of structural accommodation of trace elements in minerals, this work shows the
554 potential of using trace elements in minerals to constrain the compositional characteristics of
555 dilute gases involved in their formation and to gain insights into the gas-mediated processes that
556 lead to mineral precipitation and alteration in the shallow subvolcanic environment. This study
557 opens up new directions in the exploration of these processes.

558 ## ACKNOWLEDGEMENTS

559 The authors thank G. Lamble and J.-F. Lee for their help and expertise in the initial EXAFS
560 measurements of bulk topaz (Northrup et al., 1995) which established the foundation for our
561 current work. We appreciate Tiffany Victor's assistance in measuring some of the oxidation state
562 standards. Support for this work was provided through grants EAR1725212 (to H.N.) and EAR
563 2105876 (to H.N. and P.N.) via the Petrology and Geochemistry Program of the National
564 Science Foundation. This research used the XFM and TES beamlines of the National
565 Synchrotron Light Source II, and Beamline X15B of the National Synchrotron Light Source,
566 U.S. Department of Energy (DOE) Office of Science User Facilities operated for the DOE by
567 Brookhaven National Laboratory under Contract Nos. DE-SC0012704 and DE-AC02-

98CH10886, respectively. Measurements supported by the Tender Energy Microspectroscopy Consortium.

## REFERENCES CITED

Ackerson, M.R., Cody, G.D. and Mysen, B.O. (2020) $^{29}$Si solid state NMR and Ti K-edge XAFS pre-edge spectroscopy reveal complex behavior of Ti in silicate melts. Progress in Earth and Planetary Science, 7, 14-25.

Agangi, A., Kamenetsky, V.S., Hofmann A., Przybylowicz, W. and Vladykin, N.V. (2014) Crystallization of magmatic topaz and implications for Nb-Ta-W mineralization in F-rich silicic melts – the Ary-Bulak ongonite massif. Lithos, 202, 317-330.

Alston, N.A. and West, J. (1928) The structure of topaz. Proceedings of the Royal Society A, 121, 358-367.

Bernstein, L. and Waychunas, G. (1987) Germanium crystal chemistry in hematite and goethite from the Apex mine Utah, and some new data on germanium in aqueous solution and in stottite. Geochimica et Cosmochimica Acta, 51, 623-630.

Bikun, J.V. (1980) Fluorine and lithophile element mineralization at Spor Mountain, Utah. U.S. Department of Energy Open-File Report GJBX-225(80), 167-377.

Borisova, A.Y., Pokrovski, G.S., Pichavant, M., Freydier, R. and Candaudap, F. (2010) Arsenic enrichment in hydrous peraluminous melts: insights from femtosecond laser ablation inductively coupled plasma-quadrupole mass spectrometry, and in situ X-ray absorption fine structure spectroscopy. American Mineralogist, 95, 1095-1104.

Bove, D.J., Mast, M.A., Dalton, J.B., Wright, W.G. and Yager, D.B. (2007) Major styles of mineralization and hydrothermal alteration and related solid- and aqueous-phase geochemical signatures. In: Integrated Investigations of Environmental Effects of Historical Mining in the

591 Animas River Watershed, San Juan County, Colorado, Church, S.E., von Guerard, Paul, and
592 Finger, S.E., Eds., U.S. Geological Survey Professional Paper 1651, 165-230.

593 Breiter, K., Gardenová, N., Kanický, V. and Vaculovič, T (2013a) Gallium and germanium
594 geochemistry during magmatic fractionation and post-magmatic alteration in different types
595 of granitoids: a case study from the Bohemian Massif (Czech Republic). Geologica
596 Carpathica, 64, 171-180.

597 Breiter, K., Gardenová, N., Vaculovič, T. and Kanický, V. (2013b) Topaz as an important host
598 for Ge in granites and greisens. Mineralogical Magazine, 77, 403–417.

599 Burt, D.M. and Sheridan, M.F. (1981) A model for the formation of uranium/lithophile element
600 deposits in fluorine-enriched volcanic rocks. American Association of Petroleum Geologists
601 Studies in Geology, 13, 99-109.

602 Burt, D.M., Sheridan, M.F., Bikun, J.V. and Christiansen, E.H. (1982) Topaz rhyolites;
603 distribution, origin, and significance for exploration. Economic Geology, 77, 1818–1836.

604 Christiansen, E.H., Bikun, J.V. and Burt, D.M. (1980) Petrology and geochemistry of topaz
605 rhyolites, western United States. U.S. Department of Energy Open-File Report GJBX-
606 225(80), 37-122.

607 Christiansen E.H., Bikun, J.V., Sheridan, M.F. and Burt, D.M. (1984). Geochemical evolution of
608 topaz rhyolites from the Thomas Range and Spor Mountain, Utah. American Mineralogist,
609 69, 223-236.

610 Citrin, P.H., Northrup, P., Atkins, R.M., Glodis, P.F., Niu, L., Marcus, M.A. and Jacobson, D.C.
611 (1998) Characterizing trace metal impurities in optical waveguide materials using X-ray
612 absorption. MRS Online Proceedings Library, 524, 251-257.

Dyar, M.D., Breves, E., Gunter, M., Lanzirotti, A., Tucker, J., Carey, C., Peel, S., Brown, E. and Oberti, R. (2016) Use of multivariate analysis for synchrotron micro-XANES analysis of iron valence state in amphiboles. American Mineralogist, 101, 1171-1189.

Farges, F., Brown, G.E., Jr. and Rehr, J.J. (1997) Ti K-edge XANES studies of Ti coordination and disorder in oxide compounds: comparison between theory and experiment. Physical Review B, 56, 1809-1819.

Fridrichová, J., Bacik, P., Ertl, A., Wildner, M., Dekan, J. and Miglierini, M. (2018) Jahn-Teller distortion of $Mn^{3+}$-occupied octahedra in red beryl from Utah indicated by optical spectroscopy. Journal of Molecular Structure, 1152, 79-86.

Gauzzi, T. and Graça, L. (2018) A cathodoluminscence-assisted LA-ICP-MS study of topaz from different geological settings. Brazilian Journal of Geology, 48, 161-176.

Goad, B.E. and Černy, P. (1981) Peraluminous pegmatitic granites and their pegmatite aureoles in the Winnipeg River district, southeastern Manitoba. Canadian Mineralogist, 19, 177-194.

Groat, L.A., Turner, D.J. and Evans, R.J. (2014) Gem deposits. Treatise on Geochemistry, 13, 595-622.

James-Smith, J., Cauzid, J., Testemale, D., Liu, W., Hazemann, J.-L., Proux, O., Etschmann, B., Philippot, P., Banks, D., Williams, P. and Brugger, J. (2010) Arsenic speciation in fluid inclusions using microbeam X-ray absorption spectroscopy. American Mineralogist, 95, 921–932.

Kovalenko, V.L. and Kovalenko, N.I. (1976) Ongonites—subvolcanic analogues of rare metal lithium-fluorine granites. Joint Soviet-Mongolian Scientific Research Geol. Expedition, Transaction 15.

635 Halcrow, M.A. (2013) Jahn-Teller distortions in transition metal compounds, and their
636 importance in functional molecular and inorganic materials. Chemical Society Reviews, 42,
637 1784-1795.
638 Holfert, J. (1978) A field guide to topaz and associated minerals of Topaz Mountain, Utah. John
639 Holfert, Bountiful, UT.
640 Höll, R., Kling, M. and Schroll, E. (2007) Metallogenesis of germanium—a review. Ore
641 Geology Reviews, 30, 145–180.
642 Lindsey, D.A. (1977) Epithermal beryllium deposits in waterlaid tuff, western Utah. Economic
643 Geology, 72, 219-232.
644 Lindsey, D.A. (1982) Tertiary volcanic rocks and uranium in the Thomas Range and northern
645 Drum Mountains, Juab County, Utah. U.S. Geological Survey Professional Paper 1221.
646 Lipman, P.W., Christiansen, R.L. and Van Alstine, R.E. (1969) Retention of alkalis by calc-
647 alkalic rhyolites during crystallization and hydration. American Mineralogist, 54, 286-291.
648 Meng,Y., Hu, R., Huang, X. and Gao, J. (2017) Germanium in magnetite: a preliminary review.
649 Acta Geologica Sinica, 91, 711-726.
650 Maciag, B.J. and Brenan, J.M. (2020) Speciation of arsenic and antimony in basaltic magmas.
651 Geochimica et Cosmochimica Acta, 276, 198-218.
652
Newville, M. (2008) Fundamentals of XAFS
653
https://docs.xrayabsorption.org/tutorials/XAFS_Fundamentals.pdf
654 Northrup, P. (2019) The TES Beamline (8-BM) at NSLS-II: tender-energy spatially resolved X-
655 ray absorption spectroscopy and X-ray fluorescence imaging. Journal of Synchrotron
656 Radiation, 26, 2064-2074.

Northrup, P.A., Leinenweber, K., and Parise, J.B. (1994) The location of H in the high-pressure synthetic $Al_2SiO_4(OH)_2$ topaz analogue. American Mineralogist, 79, 401-404.

Northrup, P.A. and Reeder, R.J. (1994) Evidence for the importance of growth-surface structure to trace element incorporation in topaz. American Mineralogist, 79, 1167-1175.

Northrup, P.A., Lamble, G., Lee, J.-F. and Reeder, R.J. (1995). An XAFS study of arsenic substitution for silicon in topaz [$Al_2SiO_4(F,OH)_2$]. 1995 Goldschmidt Conference Program and Abstracts, 76.

Northrup, P.A. and Reeder, R. J. (1995) Relationship between the structure and growth morphology of topaz [$Al_2SiO_4(OH,F)_2$] using the periodic bond chain method. Journal of Crystal Growth, 156, 433-442.

O'Bannon, E.F. III and Williams, Q. (2019) A $Cr^{3+}$ luminescence study of natural topaz $Al_2SiO_4(F,OH)_2$ up to 60 GPa. American Mineralogist, 104, 1656–1662.

Pauling, L. (1928) The crystal structure of topaz. Proceedings of the National Academy of Sciences, USA, 14, 603-606.

Penfield, S.L. and Minor, J.C. (1894) On the chemical composition and related physical properties of topaz. American Journal of Science, s3-47, 387-396.

Pokrovski, G.S., Zakirov, I.V., Roux, J., Testemale, D., Hazemann, J.L., Bychkov, A.Y. and Golikova, G.V. (2002) Experimental study of arsenic speciation in vapor phase to 500°C: implications for As transport and fractionation in low-density crustal fluids and volcanic gases. Geochimica et Cosmochimica Acta, 70, 3453-3480.

Ravel, B. and Newville, M. (2005) ATHENA, ARTEMIS, HEPHAESTUS: data analysis for X-ray absorption spectroscopy using IFEFFIT. Journal of Synchrotron Radiation, 12, 537-541.

679 Ribbe, P.H. and Gibbs, G.V. (1971) The crystal structure of topaz and its relation to physical
680 properties. American Mineralogist, 56, 24-30.
681 Roedder, E., and Stalder, H.A. (1988) “Pneumatolysis" and fluid-retention evidence for crystal
682 growth from a vapor phase. In: Fluid Inclusions, Santosh, M. ed. Geological Society of India,
683 M-11, 1-12.
684 Rossman, G.R. (2011) The color of topaz. In: Topaz: Perfect Cleavage, Clifford, J., Falster,
685 A.U., Hanson, S., Liebtrau, S., Neumeier, G. and Staebler, G., eds., Lithographie, 79-85.
686 Sardi, F. and Heimann, A. (2014) Pegmatitic beryl as indicator of melt evolution: example from
687 the Velasco District, Pampeana pegmatite province, Argentina, and review of worldwide
688 occurrences. Canadian Mineralogist, 52, 1-28.
689 Schott, S., Rager, H., Schürmann, K. and Taran, M. (2003) Spectroscopic study of natural gem
690 quality “Imperial” topazes from Ouro Preto, Brazil. European Journal of Mineralogy, 15,
691 701–706.
692 Shevko, E.P., Bortnikova, S.B, Abrosimova, N.A., Kamenetsky, V.S., Bortnikova, S.P.,
693 Panin, G.L. and Zelenski M. (2018) Trace elements and minerals in fumarolic sulfur: the case
694 of Ebeko Volcano, Kuriles. Geofluids, 2018, Article ID 4586363.
695 Speer, J.A. and Gibbs, G.V. (1976) The crystal structure of synthetic titanite, $CaTiOSiO_4$, and
696 the domain textures of natural titanites. American Mineralogist, 61, 238-247.
697 Staatz, M.H. and Carr, W.J. (1964) Geology and mineral deposits of the Thomas and Dugway
698 Ranges, Juab and Tooele Counties, Utah. U.S. Geological Survey Professional Paper 415.
699 Symonds, R.B. and Reed, M.H. (1993) Calculation of multicomponent chemical equilibria in
700 gas-solid-liquid systems: calculation methods, thermochemical data and applications to

studies of high-temperature volcanic gases with examples from Mount St. Helens. American Journal of Science, 293, 758-864.

Testemale D., Pokrovski G. S. and Hazemann, J. L. (2011) Speciation of AsIII and AsV in hydrothermal fluids by in situ X-ray absorption spectroscopy. European Journal of Mineralogy, 23, 379-390.

Thomas, R. (1982) Ergebnisse der thermobarogeochemischen Untersuchungen an Flüssigkeitseinschlüssen in Mineralen der postmagmatischen Zinn-Wolfram Mineralisation des Erzgebirges. Freiberger Forschungshefte, 370.

Verweij, H. (1980) Melting and fining of arsenic-containing silicate glass batches. Ph.D. Thesis, Technische Hogeschool Eindhoven. https://doi.org/10.6100/IR95983

Wasim, M., Zafar, W., Tufail, M., Arif, M., Daud, M. and Ahmad, A. (2011) Elemental analysis of topaz from northern areas of Pakistan and assessment of induced radioactivity level after neutron irradiation for color induction. Journal of Radioanalytical and Nuclear Chemistry, 287, 821–826.

Wyckoff, R.W.G. (1969) Crystal Structures, Vol. 4, 174.

716 **FIGURE CAPTIONS**

717 **FIGURE 1.** Partial view of the topaz crystal structure. Structure parameters from Wyckoff
718 (1969). (Rendering by Crystalmaker).

719 **FIGURE 2.** Side and front view of topaz crystal (Topaz-64) as mounted for analysis. Black
720 cubic crystal is bixbyite.

721 **FIGURE 3.** XANES region of the merged XAS spectra for each analyzed trace element in topaz
722 with reference spectra for determination of oxidation state. A) Arsenic data with $As^{1-}$ in orpiment
723 measured in fluorescence; $As^{3+}$ and $As^{5+}$ as sodium salts dissolved in water and dried onto
724 cellulose paper measured in transmission. B) Germanium data; inset shows Si XANES in topaz
725 for comparison. C) Iron data with $Fe^{0}$ foil measured in transmission; $Fe^{2+}$ in siderite measured in
726 fluorescence using a defocused beam; $Fe^{3+}$ in ferrihydrite precipitated on quartz measured in
727 fluorescence. D) Manganese data with $Mn^{0}$ foil measured in transmission; $Mn^{2+}$ sulfate
728 measured in fluorescence; $Mn^{3+}$ in $Mn_2O_3$ measured in fluorescence; and $Mn^{4+}$ pyrolusite
729 measured in fluorescence. E) Titanium data. F) Gallium data.

730 **FIGURE 4.** Fourier transform of Si and Al EXAFS data compared to calculated fits. This is
731 effectively the distribution of radial distance, R, of scatterers around the absorbing atom, except
732 distances are not corrected for phase shift.

733 **FIGURE 5.** Arsenic EXAFS data compared to fit for As in the tetrahedral site of topaz plotted
734 as: (a) R, as Fig. 4., (b) k, the measured EXAFS frequencies before Fourier transform, (c) q, the
735 back-transform of measured data calculated from the same range of R used for fitting, i.e.
736 Fourier filtered for direct comparison to model fit, (d) the real component of R, an indicator of fit
737 quality.

738 **FIGURE 6.** Germanium EXAFS data and fit in R (as Fig. 4) for Ge in the tetrahedral site.

739 **FIGURE 7.** EXAFS data and fit in R (as Fig. 4) for trace elements in the topaz octahedral site

740 (a) Fe, (b) Mn, (c) Ga, (d) Ti.

741

This is the peer-reviewed, final accepted version for American Mineralogist, published by the Mineralogical Society of America.
The published version is subject to change. Cite as Authors (Year) Title. American Mineralogist, in press.
DOI: https://doi.org/10.2138/am-2022-8417. http://www.minsocam.org/

# TABLES

**TABLE 1.** Measured trace element abundance for samples Topaz-64 and Topaz-7. Mass values are calculated assuming a rectangular beam cross-section.

| | | | Concentration (ppm) | | Element Mass in Volume Analyze | |
|---|---|---|---|---|---|---|
| Trace Element | Computed Sampling Depth (μm) | Mass of Topaz Analyzed (ng) | Topaz-64 | Topaz-7 | Topaz-64 | Topaz-7 |
| As | 132 | 38 | 327(16) | 12.5(6) | 20(1) | 0.78(4) |
| Fe | 42 | 12 | 288(9) | 3.5(1) | 158(5) | 1.92(6) |
| Ga | 102 | 29 | 9.4(5) | 0.28(1) | 6.5(3) | 0.19(1) |
| Ge | 117 | 34 | 14.8(7) | 0.50(3) | 14.5(7) | 0.49(2) |
| Mn | 34 | 10 | 10(1) | 0.10(1) | 4.4(5) | 0.04(1) |
| Ti | 16 | 5 | 79(11) | 0.38(5) | 125(18) | 0.59(9) |

This is the peer-reviewed, final accepted version for American Mineralogist, published by the Mineralogical Society of America.
The published version is subject to change. Cite as Authors (Year) Title. American Mineralogist, in press.
DOI: https://doi.org/10.2138/am-2022-8417. http://www.minsocam.org/

748 **Table 2.** Cation-to-cation single-scattering path lengths out to second neighbors for Si and Al in
749 fluor-topaz. Models are recalculated from crystallographic data (Northrup et al. 1994). Si and Al
750 fits are from EXAFS data (this study), with model paths of similar length grouped together. Fit
751 parameters: change in path length ΔR, disorder parameter $\sigma^2$, and amplitude reduction $S0^2$;
752 degeneracy n is fixed. R-factor of Si fit is 0.087; Al, 0.025.

| **Si(IV) Model** | | **Si(IV) from EXAFS fit** | | | | | |
|---|---|---|---|---|---|---|---|
| Path | R (Å) | Shell | Path | n | ΔR (Å) | $\sigma^2$ (Å$^2$) | $S0^2$ |
| Si-O | 1.638(1) | 1 | Si-O | 4 | -.006(13) | .0003(23) | .97(9) |
| Si-O | 1.642(1) | | | | | | |
| Si-O | 1.642(1) | | | | | | |
| Si-O | 1.647(1) | | | | | | |
| | | | | | | | |
| Si-Al | 3.174(2) | 2 | Si-Al | 8 | -.009(26) | .0001(29) | .63(16) |
| Si-Al | 3.174(2) | | | | | | |
| Si-Al | 3.189(2) | | | | | | |
| Si-Al | 3.189(2) | | | | | | |
| Si-Al | 3.202(2) | | | | | | |
| Si-Al | 3.202(2) | | | | | | |
| Si-Al | 3.213(2) | | | | | | |
| Si-Al | 3.213(2) | | | | | | |

| **Al(III) Model** | | **Al(III) from EXAFS fit** | | | | | |
|---|---|---|---|---|---|---|---|
| Path | R (Å) | Shell | Path | n | ΔR (Å) | $\sigma^2$ (Å$^2$) | $S0^2$ |
| Al-F | 1.791(1) | 1 | Al-F | 2 | .003(11) | .002(2) | .73(8) |
| Al-F | 1.800(1) | 1 | Al-O | 4 | " | " | " |
| Al-O | 1.888(1) | | | | | | |
| Al-O | 1.895(1) | | | | | | |
| Al-O | 1.898(1) | | | | | | |
| Al-O | 1.899(1) | | | | | | |
| | | | | | | | |
| Al-Al | 2.810(2) | 2 | Al-Al | 2 | .03(4) | .002(6) | .43(25) |
| Al-Al | 2.839(2) | 2 | Al-Si | 4 | " | " | " |
| Al-Si | 3.174(2) | 2 | Al-Al | 2 | " | " | " |
| Al-Si | 3.189(2) | | | | | | |
| Al-Si | 3.202(2) | | | | | | |
| Al-Si | 3.213(2) | | | | | | |
| Al-Al | 3.427(2) | | | | | | |
| Al-Al | 3.427(2) | | | | | | |

This is the peer-reviewed, final accepted version for American Mineralogist, published by the Mineralogical Society of America.
The published version is subject to change. Cite as Authors (Year) Title. American Mineralogist, in press.
DOI: https://doi.org/10.2138/am-2022-8417. http://www.minsocam.org/

753 **Table 3.** Tetrahedral EXAFS fits, with model Si path lengths generated by Artemis FEFF
754 calculation included for comparison. Fit parameters: change in path length ΔR, disorder
755 parameter $\sigma^2$, and amplitude reduction $S0^2$; degeneracy n is fixed. R-factor of As fit is 0.021; Ge,
756 0.030.

| **Si(IV) Model** | | | **As(V)** | | | | | |
|---|---|---|---|---|---|---|---|---|
| Path | n | R (Å) | Shell | Path | n | ΔR (Å) | $\sigma^2$ (Å$^2$) | $S0^2$ |
| Si-O | 4 | 1.638-1.647 | 1 | As-O | 4 | .060(9) | .0010(19) | .83(14) |
| Si-Al | 8 | 3.174-3.213 | 2 | As-Al | 8 | .060(19) | .0001(24) | .78(34) |
| | | | **Ge(IV)** | | | | | |
| | | | 1 | Ge-O | 4 | .092(8) | -0.001(2) | .96(7) |

757

758 **Table 4.** EXAFS fits for octahedral ions, with model Al path lengths generated by Artemis FEFF
759 calculation included for comparison. Fit parameters: change in path length ΔR, disorder
760 parameter σ2, and amplitude reduction S02; degeneracy n is fixed. R-factor of Fe fit is 0.005; Ga
761 0.090; Mn 0.009; Ti 0.006.

| **Al(III) Model** | | | **Fe(III)** | | | | | |
|---|---|---|---|---|---|---|---|---|
| Path | n | R (Å) | Shell | Path | n | ΔR (Å) | $\sigma^2$ (Å$^2$) | $S0^2$ |
| Al-F | 2 | 1.791-1.800 | 1 | Fe-F | 2 | .086(6) | .00014(49) | 0.75(2) |
| Al-O | 4 | 1.888-1.899 | 1 | Fe-O | 4 | " | " | " |
| Al-Al | 2 | 2.810-2.839 | 2 | Fe-Al | 2 | .021(11) | -.0003(30) | 0.53(6) |
| Al-Si | 4 | 3.174-3.213 | 2 | Fe-Si | 4 | " | " | " |
| Al-Al | 2 | 3.427 | 2 | Fe-Al | 2 | " | " | " |
| | | | **Ga(III)** | | | | | |
| | | | 1 | Ga-F | 2 | .022(11) | .007(2) | .80(8) |
| | | | 1 | Ga-O | 4 | " | " | " |
| | | | **Mn(III)** | | | | | |

This is the peer-reviewed, final accepted version for American Mineralogist, published by the Mineralogical Society of America.
The published version is subject to change. Cite as Authors (Year) Title. American Mineralogist, in press.
DOI: https://doi.org/10.2138/am-2022-8417. http://www.minsocam.org/

| | | | | | |
|---|---|---|---|---|---|
| 1 | Mn-F | 2 | .034(20) | -0.001(4) | .52(17) |
| 1 | Mn-O | 4 | " | " | " |
| | | | **Ti(IV)** | | |
| 1a | Ti-F | 2 | .042(24) | .0022(69) | .60(20) |
| 1b | Ti-O | 4 | .113(24) | .0022(69) | .60(20) |

762

763

This is the peer-reviewed, final accepted version for American Mineralogist, published by the Mineralogical Society of America.
The published version is subject to change. Cite as Authors (Year) Title. American Mineralogist, in press.
DOI: https://doi.org/10.2138/am-2022-8417. http://www.minsocam.org/

764 **FIGURE 1.**

765
766
767
768

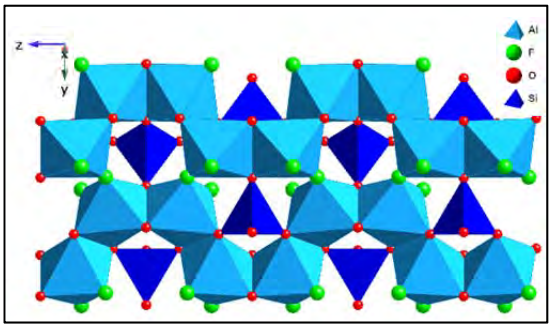


769

770 **FIGURE 2.**

771
772
773
774

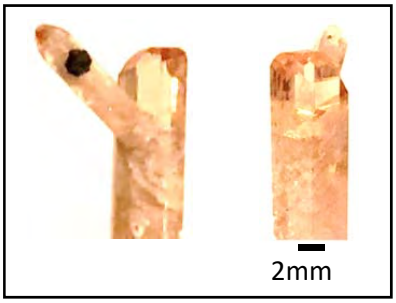


775
776
777
778
779
780
781

This is the peer-reviewed, final accepted version for American Mineralogist, published by the Mineralogical Society of America.
The published version is subject to change. Cite as Authors (Year) Title. American Mineralogist, in press.
DOI: https://doi.org/10.2138/am-2022-8417. http://www.minsocam.org/

782 **FIGURE 3.**

783

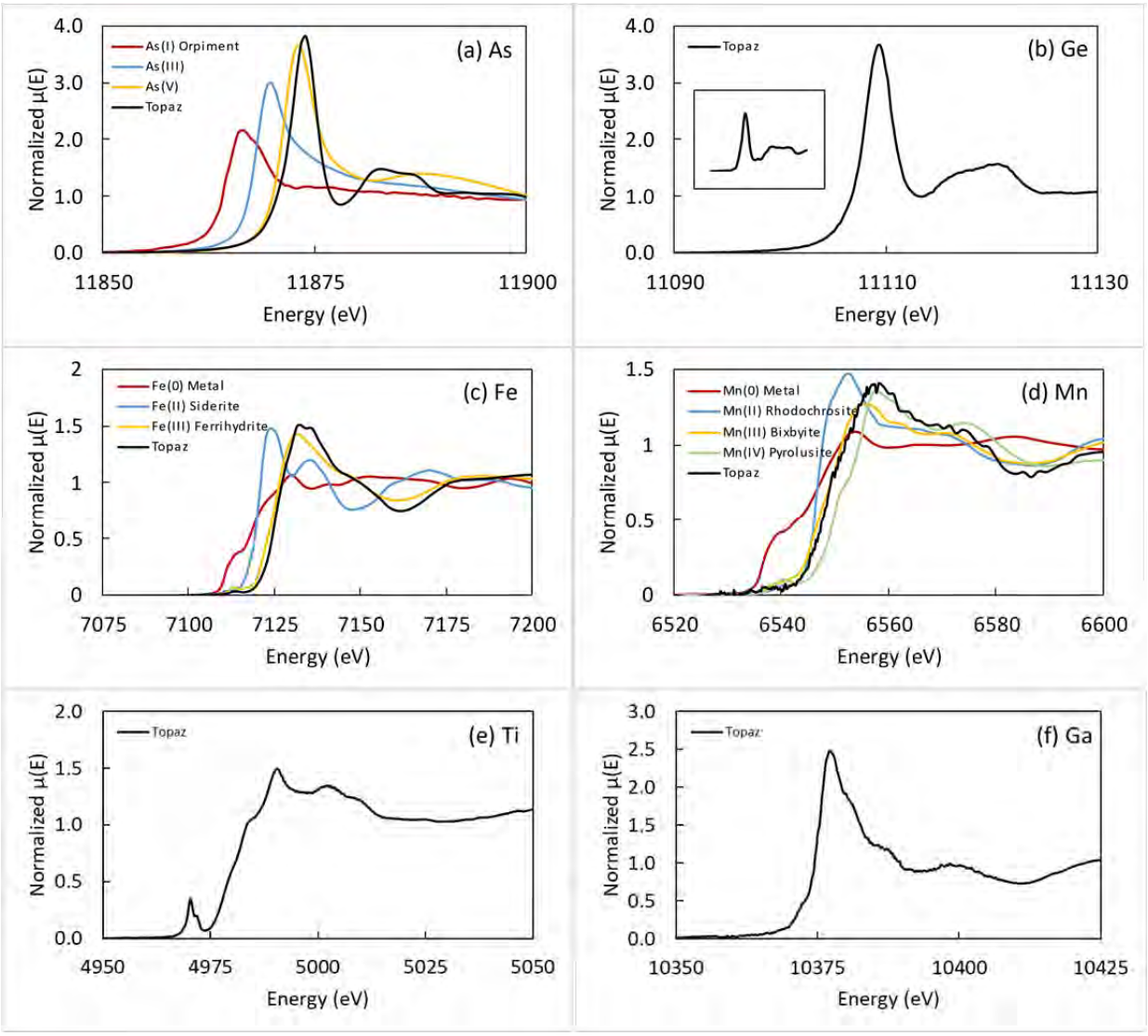


784

785

786

This is the peer-reviewed, final accepted version for American Mineralogist, published by the Mineralogical Society of America.
The published version is subject to change. Cite as Authors (Year) Title. American Mineralogist, in press.
DOI: https://doi.org/10.2138/am-2022-8417. http://www.minsocam.org/

787 **FIGURE 4.**

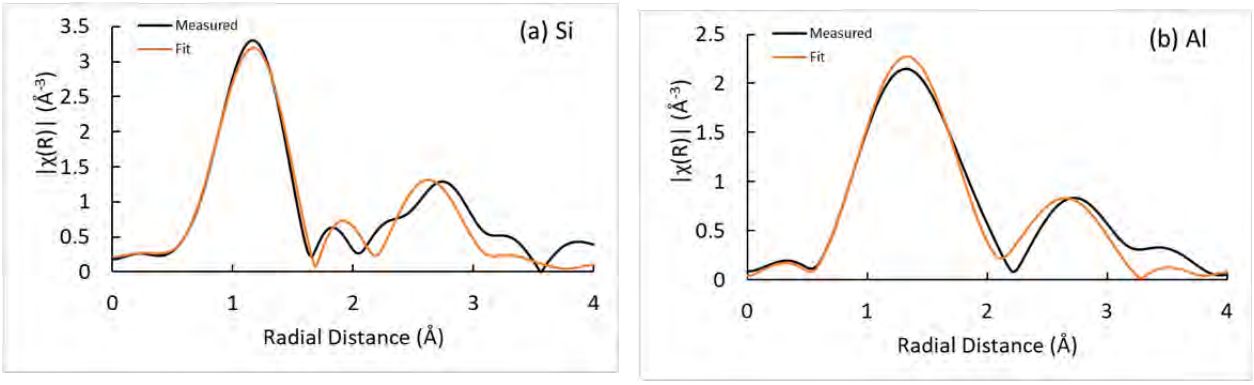


788

789 **FIGURE 5.**

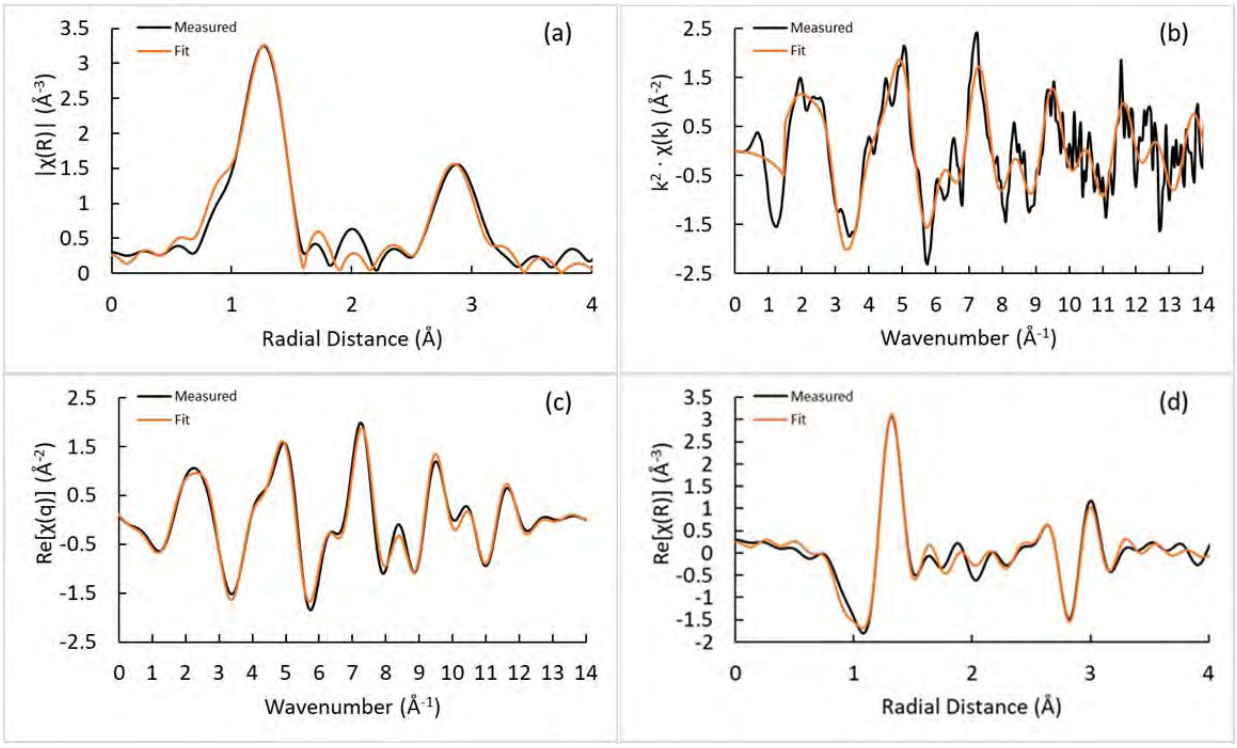


790

791

792

This is the peer-reviewed, final accepted version for American Mineralogist, published by the Mineralogical Society of America.
The published version is subject to change. Cite as Authors (Year) Title. American Mineralogist, in press.
DOI: https://doi.org/10.2138/am-2022-8417. http://www.minsocam.org/

793 **FIGURE 6.**

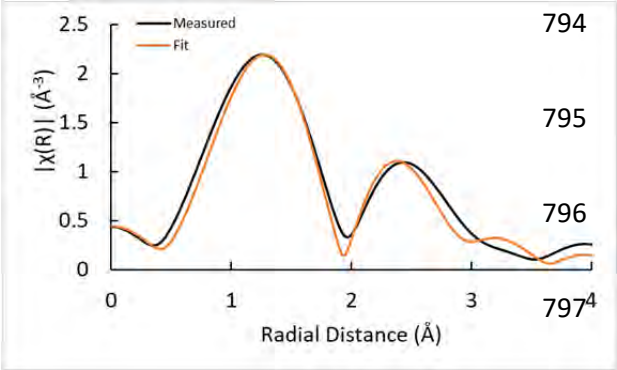


794
795
796
797

798

799 **FIGURE 7.**

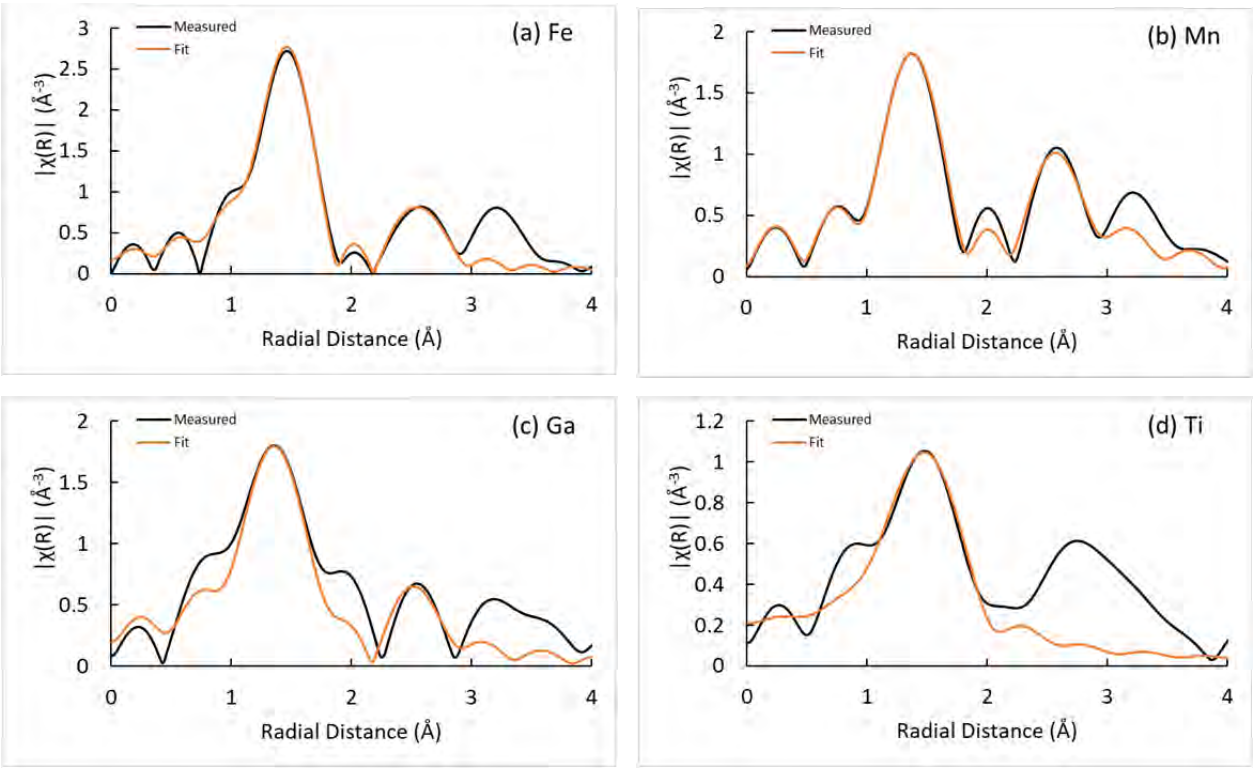


800